https://doi.org/10.5194/egusphere-2026-4530
Preprint. Discussion started: 5 November 2026
© Author(s) 2026. CC BY 4.0 License.

Reconciling Arctic sea ice roughness across four observing platforms: a resolution transfer function and the stability of spectral shape over six decades

Lei Yang[1] and Lin Zhu[2]

[1]Key Laboratory of Marine Science and Numerical Modeling, First Institute of Oceanography, Ministry of Natural Resources, Qingdao 266061, China
[2]Institute of Oceanographic Instrumentation, Qilu University of Technology (Shandong Academy of Sciences), Qingdao 266101, China

Correspondence: Lei Yang (leiyang@fio.org.cn)

Abstract. Sea ice roughness is measured by platforms whose spatial resolutions differ by two orders of magnitude, and the resulting estimates disagree by a factor of four, which has prevented the assembly of a consistent long-term record. Here we analyse ice topography from four platforms within a single broken power law spectral framework: submarine upward-looking sonar (5470 profiles, 43 cruises, 1960–2005), MOSAiC airborne laser scanning (55 256 transects), under-ice remotely operated vehicle (ROV) multibeam (52 264 transects from 36 dives), and ICESat-2 altimetry (25 740 segments). The fourfold spread in the slope-to-amplitude ratio z_2/z_1 collapses onto a single resolution degradation curve, $z_2/z_1 = 0.218\,\Delta x^{-0.46}$ ($R^2 = 0.92$), whose exponent follows analytically from the observed spectral shape rather than being fitted freely; the curve provides a transfer function for inter-calibrating roughness estimates between platforms with effective footprints of 0.5–20 m. The resolution-independent spectral parameters ($\beta_1 \approx -0.5$, $\beta_2 \approx -2.2$, $\lambda_{\mathrm{break}} \approx 99$ m) are consistent across all four platforms and both ice surfaces, and show no significant trend over the 45-year submarine record despite a halving of mean ice thickness, although that record can only exclude changes larger than about 160 % of the median exponent at 80 % power. Eighty-five paired surface–bottom observations spanning a full MOSAiC year show that the isostatic approximation holds at the derivative level (z_2/z_1 surface-to-bottom ratio 0.99 ± 0.14, against 0.28 for the amplitude z_1), so under-ice morphology can be inferred from satellite surface measurements. That fidelity is seasonal: the ratio is 0.94 ± 0.07 from October to May but reverses to 1.14 ± 0.10 from June to September, when surface melt and basal melt together leave the surface sharper than the underside. Roughness amplitude and spectral shape therefore respond to forcing on different terms: z_1 varies sevenfold over the seasonal cycle and has declined with the ice cover, while the shape parameters remain stable to within the tested bounds.

1 Introduction

Arctic sea ice has thinned by approximately half since the 1960s, with September extent declining from ∼7.5 to below 4 million km^2 and the fraction of multi-year ice dropping from over 60 % to less than 30 % (Kwok, 2018; Stroeve and Notz, 2018; Kwok and Rothrock, 2009; Lindsay and Schweiger, 2015). This transformation has profound consequences for the ocean–atmosphere momentum exchange, which is mediated by the roughness of both the ice surface and its underside. Surface

https://doi.org/10.5194/egusphere-2026-4530
Preprint. Discussion started: 5 November 2026
© Author(s) 2026. CC BY 4.0 License.

roughness governs the aerodynamic form drag that couples wind stress to ice motion, while bottom roughness determines the oceanic form drag through which the ocean current drives or retards the ice pack (Tsamados et al., 2014). Together, these drag terms set the momentum flux from the atmosphere through the ice into the ocean, and with it ice drift speed and deformation rate (Castellani et al., 2014; Martin et al., 2016). Recent analyses suggest that as multi-year ice has been replaced by smoother first-year ice, the aerodynamic drag coefficient has decreased (Krumpen et al., 2025).

Roughness also enters directly into the retrieval of ice thickness from satellite altimetry. Both CryoSat-2 radar altimetry and ICESat-2 photon-counting lidar convert measured freeboard to thickness using the isostatic assumption, which requires knowledge of how the ice surface geometry relates to its underside (Kwok and Cunningham, 2008). Inadequate treatment of roughness has been identified as a leading source of systematic error in these retrievals, contributing 20–30 % uncertainty in CryoSat-2 thickness estimates (Landy et al., 2020). Despite its importance, the characterization of sea ice roughness has relied for decades on a single statistical parameter, the root-mean-square height z_1 (equivalently, σ_h). This measure captures the amplitude of topographic variations but not their spatial organization: surfaces with identical z_1 can range from fields of sharp pressure ridges to broad, gentle undulations (Castellani et al., 2014).

The spectral decomposition of ice draft profiles provides a richer and resolution-independent description that separates the contributions of different spatial scales. Rothrock and Thorndike (1980) established that the power spectral density (PSD) of under-ice topography falls approximately as the inverse cube of wavenumber at high wavenumbers, and Goff (1995) showed that a draft profile is reproduced by a stochastic model requiring a characteristic length and a fractal dimension alongside an amplitude. Both descriptions imply that a single scaling law cannot hold across all scales, but neither resolves where the transition lies. We find that the spectrum is well described by a broken power law: a shallow slope β_1 at wavelengths longer than a characteristic break scale $\lambda_{\mathrm{break}} \approx 99$ m, steepening to β_2 at shorter wavelengths. The break wavelength corresponds roughly to the width of individual pressure ridges or the spacing between adjacent keels, separating the organized ridge-field regime from the intra-ridge block texture; that it is a real feature of the spectra rather than an artefact of fitting two lines to a curve is established against matched single-power-law surrogates in the Supplement (Fig. S1). Early submarine draft surveys characterized the ice cover through keel spacing and draft distributions rather than spectra (Wadhams and Horne, 1980), and later spectral work was limited to individual cruises without systematic cross-platform or temporal comparison. Unlike z_1, the spectral parameters β_1, β_2, and λ_{break} characterize the shape of the roughness spectrum rather than its amplitude. In the analogy of sound, they describe the timbre of the ice morphology, as distinct from its loudness.

The practical obstacle to assembling a consistent long-term roughness record is that the available platforms sample the ice at spatial resolutions differing by two orders of magnitude. The commonly used parameter z_2/z_1 (the ratio of RMS slope to RMS height) varies by a factor of four among them, from $\sim$0.23 at the 0.5 m resolution of airborne and under-ice laser and sonar mapping to $\sim$0.05 at the $\sim$20 m effective footprint of ICESat-2. Whether this spread reflects genuine morphological differences or merely the spatial averaging imposed by each sensor has not been established, and until it is, measurements from different platforms cannot be combined. The same problem has been confronted, and solved, in the study of fault surface roughness: Candela et al. (2012) showed that multi-instrument measurements spanning nine orders of magnitude in scale collapse onto a single self-affine model once resolution effects are accounted for. Molecular-dynamics simulations of plastically

https://doi.org/10.5194/egusphere-2026-4530
Preprint. Discussion started: 5 November 2026
© Author(s) 2026. CC BY 4.0 License.

deformed solids have further shown that self-affine roughness emerges from spatially correlated deformation (Hinkle et al., 2020), suggesting that a similar unification may be achievable for sea ice, whose topography is likewise built by the fracture and piling of ice blocks (Hopkins, 1998).

Despite six decades of submarine sonar measurements and the recent addition of airborne laser scanning (ALS), remotely operated vehicle (ROV) multibeam sonar, and satellite laser altimetry (ICESat-2), no prior study has systematically compared spectral morphology across these platforms, or tested how it has responded as the ice cover has thinned (Rothrock et al., 2008; Hutter et al., 2023; Anhaus et al., 2025; Nicolaus et al., 2022; Petty et al., 2016). A recent analysis of the same submarine dataset classified individual keel cross-sections by geometric type (Eilers and Bradley, 2026); our approach is complementary, characterizing the aggregate spectral shape of the entire draft profile rather than the geometry of individual ridges.

Here we bring four observing platforms into a single spectral framework and ask whether their apparent disagreement is geophysical or instrumental (Fig. 1). We analyse 5470 draft profiles from 43 submarine cruises (1960–2005), 55 256 surface elevation transects from 63 helicopter ALS flights during MOSAiC (2019–2020), 52 264 under-ice transects from 36 ROV multibeam dives yielding 85 quasi-simultaneous ALS–ROV pairs, and 25 740 along-track segments from ICESat-2. We show that the fourfold cross-platform spread in z_2/z_1 collapses onto a single resolution degradation curve that follows analytically from the broken power law, and we give the resulting transfer function for inter-calibration. We then use the resolution-independent spectral exponents, which are immune to this artefact, to test whether the shape of the roughness spectrum changed over the 45 years of the submarine record, and we quantify the change that record was capable of detecting. Finally, we show that the isostatic relation between the ice surface and its underside holds at the level of the first spatial derivative during the freeze season, which is the condition under which under-ice morphology can be inferred from satellite surface measurements, and that it breaks down in the melt season when the surface becomes sharper than the underside.

2 Data

We combine four independent observations of sea ice topography whose effective spatial resolutions span 0.5 to ∼20 m and whose observation periods together cover 1960–2020 (Fig. 1). Two of them sense the ice underside (submarine sonar, ROV multibeam) and two the upper surface (ALS, ICESat-2).

2.1 Submarine upward-looking sonar

Under-ice draft profiles were obtained from the NSIDC G01360 archive (National Snow and Ice Data Center, 1998; Rothrock et al., 2008), comprising 43 cruises conducted by US, UK, and SCICEX submarines between 1960 and 2005. Each cruise yielded multiple along-track segments of continuous upward-looking sonar (ULS) draft measurements, with sampling intervals ranging from 1.0 to 3.5 m depending on vessel speed and digitization rate. A total of 5470 segments longer than 256 points were retained for spectral analysis. The temporal sampling of the archive is non-uniform: of the 43 cruises, 5 fall in the 1970s, 15 in the 1980s, and 17 in the 1990s, but only 3 each in the 1960s and 2000s.

https://doi.org/10.5194/egusphere-2026-4530
Preprint. Discussion started: 5 November 2026
© Author(s) 2026. CC BY 4.0 License.

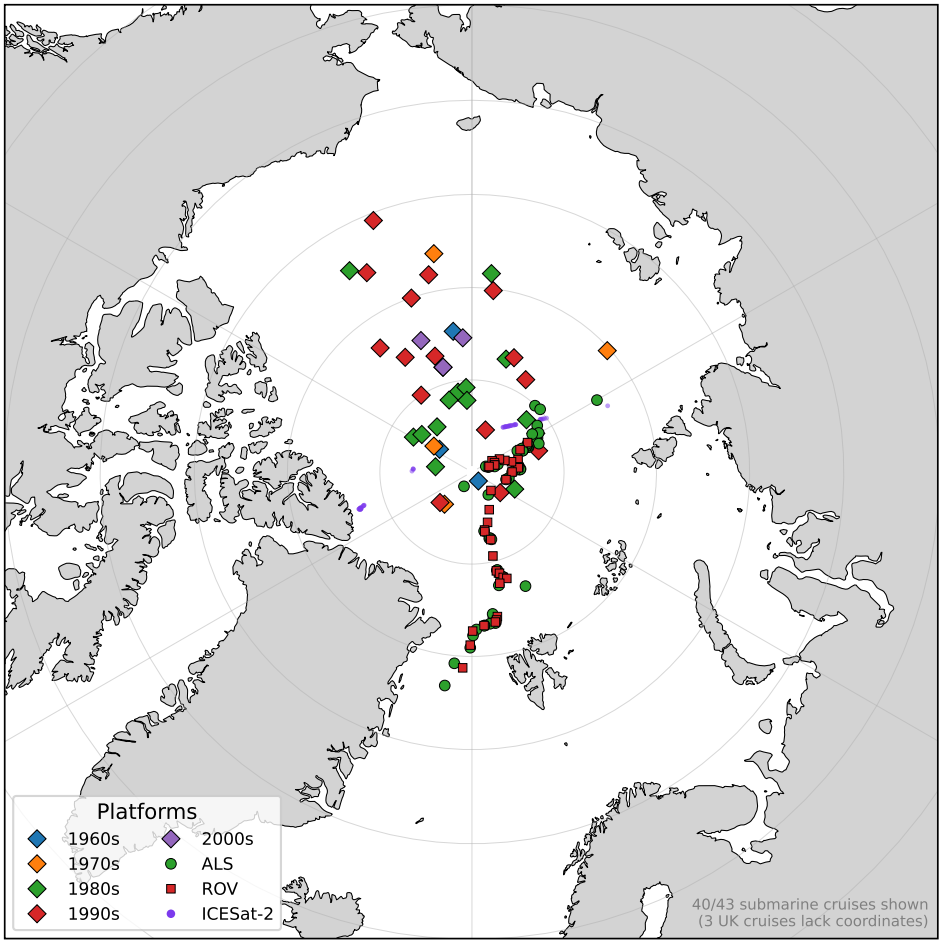


Figure 1. Spatial coverage of the four observing platforms. Polar stereographic map showing submarine cruise median positions (1960–2005, diamonds coloured by decade), MOSAiC ALS helicopter flights (2019–2020, green circles), ROV dive sites (red squares), and ICESat-2 ground tracks (purple dots). Three of the 43 submarine cruises (UK76, UK87, UK91) are omitted because coordinates are not available in the distributed segment table; they are retained in all statistical analyses.

2.2 MOSAiC airborne laser scanner

Helicopter-borne laser scanner (ALS) surveys of ice surface elevation were acquired during MOSAiC legs 1–5 (September 2019 to September 2020) at 0.5 m grid resolution (Hutter et al., 2023; Nicolaus et al., 2022). We processed 63 flights (PANGAEA 950339), extracting one-dimensional transects along grid rows and columns with a minimum contiguous length of 200 m. Freeboard was computed as $h_{\mathrm{fb}} = h_{\mathrm{elev}} - h_{\mathrm{ssh}}$, where h_{ssh} is the local instantaneous sea surface height derived from open-water tie points. For flights lacking a pre-computed freeboard variable, we computed it directly from the elevation and

https://doi.org/10.5194/egusphere-2026-4530
Preprint. Discussion started: 5 November 2026
© Author(s) 2026. CC BY 4.0 License.

sea surface height fields. Transects were resampled to a uniform 2 m spacing and randomly subsampled under a per-flight cap, producing 55 256 transects in total.

2.3 MOSAiC ROV multibeam sonar

Under-ice draft grids at 0.5 m (standard) and 0.1 m (high-resolution) spacing were obtained from ROV multibeam surveys during MOSAiC (Anhaus et al., 2025, 2024). The archive provides 38 gridded products covering 36 unique dive events across legs 2–5 (31 December 2019 to 17 September 2020), so the ROV record spans freeze-up, midwinter, and melt. We extracted one-dimensional transects along grid rows and columns with a minimum length of 60 m and resampled to 2 m spacing, applying the same spectral analysis as for the ALS and submarine data, which yields 52 264 transects. The two 0.1 m high-resolution grids contribute no transects because their spatial extent is too small to survive resampling to the common 2 m grid; the corresponding dives are represented by their standard-resolution products. Spatial positions for each dive are taken from the *Polarstern* ship position recorded in the event metadata.

2.4 ICESat-2 satellite altimetry

Along-track sea ice surface heights from ICESat-2 ATL07 version 007 (Kwok et al., 2025; Markus et al., 2017; Luthcke et al., 2021) were accessed via NASA Earthdata using cloud-based streaming (`earthaccess`), avoiding the need to download full granule files (∼600 MB each). We processed 29 granules spanning October 2019 to September 2020, extracting 25 740 transects across all six beams. The ATL07 product provides segment-level heights at a median along-track spacing of 6.8 m, each derived from ∼150 signal photons. Only segments flagged as sea ice with quality flag 1 and SSH flag 0 were retained. Sensitivity analysis indicates that the effective footprint of ATL07 segments is ∼20 m (best fit to the ALS degradation curve of Sect. 3.4), larger than the nominal segment spacing because of the multi-photon averaging inherent in the segment-fitting algorithm. A separate multi-season sample of 8878 transects from five freeze seasons (2018–2023) was compiled to test whether the morphology parameters are stable across years.

3 Methods

3.1 Morphology parameters

For a detrended ice topography profile $h(x)$ of length L sampled at interval Δx, we define three morphology parameters that characterize successively higher-order spatial structure:

$$z_1 = \sqrt{\frac{1}{N}\sum_{i=1}^{N} h_i^2}, \quad z_2 = \sqrt{\frac{1}{N-2}\sum_{i=2}^{N-1}\left(\frac{h_{i+1}-h_{i-1}}{2\Delta x}\right)^2}, \quad z_3 = \sqrt{\frac{1}{N-2}\sum_{i=2}^{N-1}\left(\frac{h_{i+1}-2h_i+h_{i-1}}{\Delta x^2}\right)^2}, \tag{1}$$

where z_1 is the root-mean-square (RMS) height, z_2 the RMS slope (first derivative), and z_3 the RMS curvature (second derivative), originally introduced for machined surfaces by Myers (1962). The ratio z_2/z_1 measures the steepness of the topography relative to its amplitude: a surface with sharp, narrow features has high z_2/z_1, while a surface with broad, gentle undulations

https://doi.org/10.5194/egusphere-2026-4530
Preprint. Discussion started: 5 November 2026
© Author(s) 2026. CC BY 4.0 License.

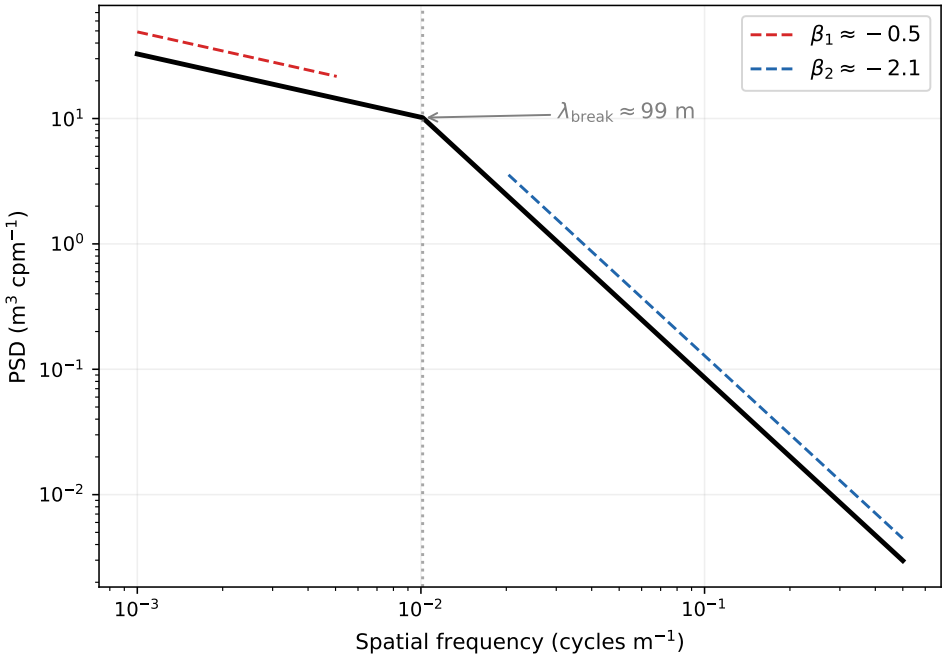


Figure 2. The broken power law model of Eq. (2), drawn with the exponents observed in this study: $\beta_1 \approx -0.5$ at wavelengths longer than the break and $\beta_2 \approx -2.1$ at shorter wavelengths (cruise-level medians; the pooled median β_2 is -2.2), separated at $\lambda_{\text{break}} \approx 99$ m. Dashed lines show the two asymptotic power laws, offset vertically for legibility.

has low z_2/z_1. Because z_1 is a length and z_2 is dimensionless, the ratio carries dimensions of inverse length. That is the root of the resolution dependence developed in Sect. 3.3: for a surface with no intrinsic scale in the measured band, a quantity carrying an inverse-length dimension can only be set by the bandwidth limits themselves, the record length and the sampling interval. A genuinely dimensionless descriptor, such as a spectral exponent, is free of them. The analyses below use z_1, z_2/z_1, and the spectral parameters; z_3 is defined for completeness but is not analysed further. All profiles were linearly detrended before computing these quantities or estimating spectra, to remove large-scale gradients associated with regional ice thickness variations.

3.2 Spectral model and estimation

The one-sided power spectral density (PSD) $S(f)$ of detrended profiles was estimated using Welch's method with a Hann window (segment length $\min(N, 512)$ points, 50 % overlap). The PSD was log-binned into 21 geometrically spaced frequency bands to reduce noise in the log-log domain.

https://doi.org/10.5194/egusphere-2026-4530
Preprint. Discussion started: 5 November 2026
© Author(s) 2026. CC BY 4.0 License.

We model $S(f)$ as a broken power law with two spectral regimes (Fig. 2):

$$S(f) = \begin{cases} A\, f^{\beta_1} & f < f_{\mathrm{break}} \\ A\, f_{\mathrm{break}}^{\beta_1-\beta_2}\, f^{\beta_2} & f \geq f_{\mathrm{break}} \end{cases} \tag{2}$$

where β_1 is the low-frequency (large-scale) spectral exponent, β_2 is the high-frequency (small-scale) exponent, f_{break} is the break frequency, and $\lambda_{\mathrm{break}} = 1/f_{\mathrm{break}}$ is the corresponding break wavelength. The break was located by exhaustive search: for each candidate break point k in the log-binned spectrum, separate linear regressions were performed on the $\log f$–$\log S$ values below and above f_k, and the break minimizing the total sum of squared residuals was selected.

Because this procedure will report some slope change even for a spectrum that has none, we calibrated it against matched single-power-law surrogate profiles processed through the identical pipeline. The observed slope change is 2.31 times the null value, and 64 % of observed breaks fall in the 50–200 m band expected for ridge spacing against 10 % of null breaks, which pile up at the edge of the analysis band (Fig. S1). The ratio is stable between 2.21 and 2.25 for bin counts from 20 to 34, so the 21 bins used here are not a special case (Fig. S2).

3.3 Why z_2/z_1 depends on sensor resolution

The connection between the morphology parameters (Eq. 1) and the spectral model (Eq. 2) follows from Parseval's theorem:

$$z_1^2 = \int_0^{f_{\max}} S(f)\,\mathrm{d}f, \qquad z_2^2 = \int_0^{f_{\max}} (2\pi f)^2\, S(f)\,\mathrm{d}f. \tag{3}$$

For a given spectral shape (β_1, β_2, λ_{break}), the ratio z_2/z_1 is a deterministic function of the bandwidth limits $[1/L,\ 1/(2\Delta x)]$. Changing the sensor resolution Δx shifts the upper integration limit, altering z_2/z_1 even though the underlying spectrum is unchanged. Platforms with different effective footprints will therefore measure different z_2/z_1 values from the same ice, as a mathematical consequence of bandwidth truncation rather than a physical difference in morphology. The resolution-independent parameters β_1, β_2, and λ_{break} are not subject to this effect and are therefore the appropriate quantities for cross-platform and cross-era comparison.

In the asymptotic regime where the sensor resolves wavelengths well below the break ($\Delta x \ll \lambda_{\mathrm{break}}/2$), the variance integral is dominated by the low-frequency regime and saturates, while the slope-variance integral is dominated by the high-frequency regime and scales as $f_{\max}^{\beta_2+3}$. The ratio therefore simplifies to

$$z_2/z_1 \;\propto\; f_{\max}^{(\beta_2+3)/2} \;=\; (2\Delta x)^{-(\beta_2+3)/2}, \tag{4}$$

predicting a power-law degradation curve with exponent $-(\beta_2+3)/2$. Substituting the observed median $\beta_2 = -2.09$ yields an exponent of -0.46, which matches the empirical fit obtained below (Eq. 5) to within the rounding precision. This asymptotic result is valid for $\Delta x \lesssim \lambda_{\mathrm{break}}/6 \approx 16$ m; at coarser resolutions the full integral (evaluated numerically) predicts a steepening toward the β_1-regime exponent of -1, a testable prediction for future low-resolution sensors. Over the 1–20 m range relevant to existing platforms, the full integral yields an equivalent exponent of -0.48, within 5 % of the empirical value (Fig. S3).

https://doi.org/10.5194/egusphere-2026-4530
Preprint. Discussion started: 5 November 2026
© Author(s) 2026. CC BY 4.0 License.

The degradation curve is therefore not an ad hoc empirical fit but a direct mathematical consequence of the broken power law spectral shape.

The same bandwidth argument applies to the lower integration limit set by the record length. Median z_2/z_1 falls from 0.137 in the shortest quartile of submarine segments to 0.099 in the longest (Fig. S7), which is a further reason to base cross-platform and cross-era comparisons on the exponents rather than on z_2/z_1.

3.4 Resolution degradation experiment

To test whether cross-platform differences in z_2/z_1 are attributable to sensor resolution, we progressively smoothed the 0.5 m ALS freeboard grids using two kernel types: isotropic Gaussian ($\sigma = d_{\mathrm{fp}}/2.355$) and uniform boxcar ($w = d_{\mathrm{fp}}$), where d_{fp} is the target footprint diameter. Smoothed grids were processed through the same transect extraction and spectral analysis pipeline. The experiment was performed at eight target footprints (0.5, 1, 2, 4, 6, 10, 20, 50 m) on three independent ALS datasets (flights 950446, 950455, 950460), yielding 1000 transects per dataset per footprint. The difference between the Gaussian and boxcar results establishes an uncertainty envelope for the degradation curve, since the real sonar and lidar footprint functions are neither exactly Gaussian nor exactly uniform.

3.5 ALS–ROV pairing

Quasi-simultaneous surface–bottom pairs were identified by matching ALS flights with ROV dives within ± 7 days and 50 km, using the ALS flight centre coordinates and the *Polarstern* ship position for each ROV event. This yielded 85 pairs spanning 24 December 2019 to 19 September 2020, so the comparison covers both the freeze season and the melt season. For each pair, flight- and dive-level median values of z_1 and z_2/z_1 were compared.

The 85 pairs are not 85 independent observations: they are formed from 28 unique ROV dives and 45 unique ALS flights, with 1–7 pairs drawn from each ROV dive. We therefore report the paired ratios both pooled over pairs and aggregated to one value per ROV dive, so that the dispersion is not understated by treating repeated use of the same dive as replication. Pairs are additionally split into freeze (October–May) and melt (June–September) subsets on the ROV dive date.

3.6 Trend analysis and confound controls

Temporal trends in spectral parameters were assessed at the cruise-median level ($n = 43$) to mitigate spatial autocorrelation among segments within a single cruise track. Both Pearson linear regression and Spearman rank correlation were applied. Robustness was tested by repeating the analysis after excluding the two 1960 cruises, which act as leverage points because of their temporal isolation. The minimum detectable effect (MDE) at 80 % power was estimated as $\mathrm{MDE}_{\mathrm{slope}} = (z_{\alpha/2} + z_{\beta}) \cdot \sigma_{\mathrm{residual}}/(\sqrt{n} \cdot \mathrm{SD}_{\mathrm{years}})$, where $z_{\alpha/2} = 1.96$ and $z_{\beta} = 0.84$. Because the archive spans only 43 cruises with uneven temporal coverage, this bound is an essential companion to any null result and is reported alongside it throughout.

Two confounds require control. First, the native sampling interval d_x differs among cruises and is correlated with z_2/z_1 ($r = -0.64$, $p < 10^{-4}$; Fig. A1a), so apparent temporal changes in z_2/z_1 could be instrumental. The spectral parameters

https://doi.org/10.5194/egusphere-2026-4530
Preprint. Discussion started: 5 November 2026
© Author(s) 2026. CC BY 4.0 License.

also correlate with d_x across cruises (λ_{break}: $r = +0.76$; β_1: $r = +0.53$; β_2: $r = +0.33$), reflecting bandwidth truncation in finite-record fitting rather than a physical dependence on sensor spacing. However, d_x exhibits no temporal drift ($r = -0.14$, $p = 0.36$), and partial correlations controlling for d_x leave all trend conclusions unchanged (β_2 vs. year: $r = -0.06$, $p = 0.72$; λ_{break} vs. year: $r = -0.42$, $p = 0.005$; Fig. S5). Second, a regional sampling confound exists because early cruises favoured different Arctic sectors than later SCICEX missions. At the cruise-median level, β_2 does not differ significantly among regions (Kruskal–Wallis $p = 0.22$), while β_1 ($p = 0.02$) and λ_{break} ($p = 0.03$) show marginal differences. A segment-level stress test over seven region–ice-type classes shows that the marginal regional signal is carried entirely by the two smallest and least well characterised groups; dropping them removes it ($p = 0.91$), and among multi-year ice regions alone there is none ($p = 0.67$; Fig. S6). The partial correlations controlling for d_x additionally absorb much of this confound, because resolution and region co-vary with cruise identity.

Uncertainty on the pooled Hurst exponent was obtained by cluster bootstrap, resampling whole cruises rather than segments so that within-cruise autocorrelation is respected ($n = 43$ cruises, 5470 segments, 10 000 resamples; Fig. S4).

4 Results

4.1 Spectral form across platforms

Representative profiles from each platform illustrate the range of roughness amplitudes and resolutions sampled by the four datasets (Fig. 3). The RMS height differs by an order of magnitude between the submarine draft profiles ($z_1 \approx 1.9$ m) and the ICESat-2 surface heights ($z_1 \approx 0.18$ m), as expected given that the two sense opposite sides of the ice and at very different footprints. The spectral form, however, is common to both: a broken power law with a shallow low-frequency exponent and a steep high-frequency exponent separated by a break near 100 m (Fig. 4). ICESat-2 recovers the break at $\lambda_{\mathrm{break}} \approx 82$ m and $\beta_1 \approx -0.6$, independently of the submarine estimate, although its high-frequency exponent is unreliable because the spectrum is attenuated below the $\sim$7 m segment spacing.

4.2 Sensor resolution explains the cross-platform spread

The morphology parameter z_2/z_1 varies by a factor of four across platforms, from 0.232 (ROV multibeam at 0.5 m resolution, 36 dives) and 0.226 (ALS at 0.5 m, 63 flights) to 0.132 (submarine sonar at $\sim$6 m effective beam width) and 0.056 (ICESat-2 ATL07 at $\sim$20 m effective footprint; Fig. 5a). The ordering follows sensor resolution exactly, and the two platforms that share a resolution (ALS and ROV, 0.5 m) agree to within 3 % despite sensing opposite sides of the ice.

We tested the resolution explanation directly by progressively smoothing the 0.5 m ALS freeboard grids to eight target footprints between 0.5 and 50 m (Sect. 3.4). The Gaussian-smoothed ALS data reproduce the submarine value at a 6 m footprint ($z_2/z_1 = 0.117$, within 13 % of the submarine measurement of 0.132, inside the kernel uncertainty quantified below). The ICESat-2 measurement falls on the same degradation curve at an effective footprint of approximately 20 m (Fig. 5b). The ICESat-2 footprint was itself calibrated against this curve, so the independent support from ICESat-2 comes instead

https://doi.org/10.5194/egusphere-2026-4530
Preprint. Discussion started: 5 November 2026
© Author(s) 2026. CC BY 4.0 License.

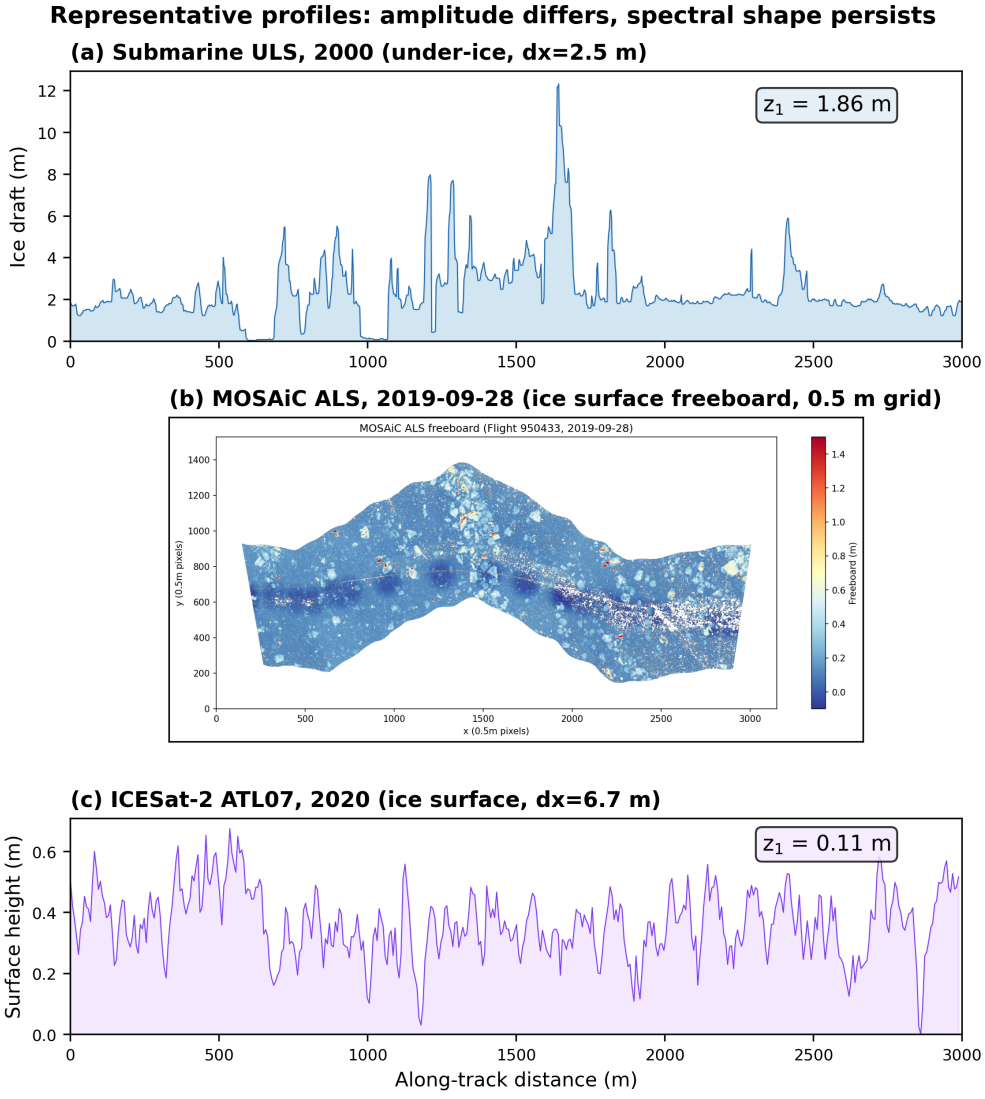


Figure 3. Three observing platforms at different resolutions and scales. (a) Submarine upward-looking sonar profile of ice draft from 2000 ($z_1 = 1.87$ m, sampling interval 2.5 m). (b) MOSAiC helicopter-borne laser scanner (ALS) freeboard map at 0.5 m grid resolution, showing pressure ridges (red), level ice (yellow-blue), and leads (dark). (c) ICESat-2 ATL07 along-track surface height from October 2019 ($z_1 = 0.18$ m, native segment spacing 5.8 m). Despite the order-of-magnitude difference in roughness amplitude, the spectral shape (Fig. 4) is consistent across all three platforms.

from its recovery of the break wavelength ($\lambda_{\text{break}} \approx 82$ m) and low-frequency exponent ($\beta_1 \approx -0.6$), which are resolution-independent. Three independent ALS datasets (flights on 7 January, 21 January, and 9 February 2020) yield nearly identical degradation curves, with a standard deviation below 0.01 across all footprints.

https://doi.org/10.5194/egusphere-2026-4530
Preprint. Discussion started: 5 November 2026
© Author(s) 2026. CC BY 4.0 License.

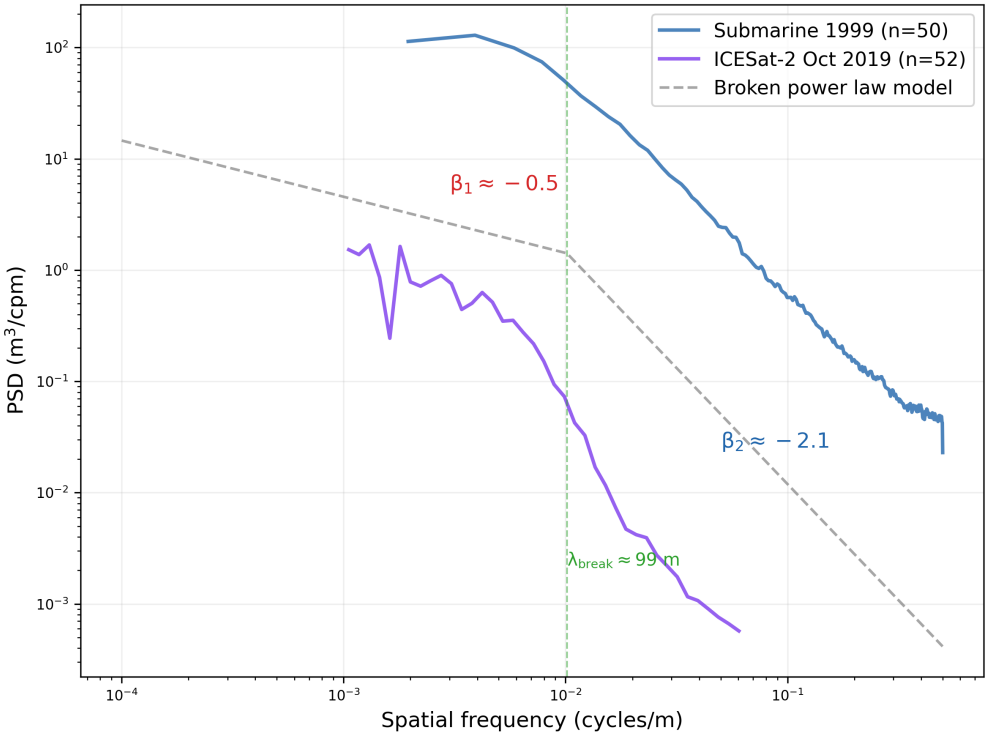


Figure 4. Power spectral density of ice topography from submarine sonar (1999, blue; $n = 50$ segment average) and ICESat-2 ATL07 (October 2019, purple; $n = 52$ transects at native ∼7 m segment spacing). The dashed grey line shows the broken power law with $\beta_1 \approx -0.5$ and $\beta_2 \approx -2.1$ (cruise-level median; pooled median -2.2). The green dashed line marks the break wavelength $\lambda_{\mathrm{break}} \approx 99$ m. ICESat-2 independently resolves the break ($\lambda \approx 82$ m) and the low-frequency exponent ($\beta_1 \approx -0.6$); at high frequencies the ICESat-2 spectrum is attenuated below its native ∼7 m segment spacing, so spectral exponents from ICESat-2 are reliable only for the break and the low-frequency regime.

The choice of smoothing kernel introduces systematic uncertainty: at a 6 m footprint, the boxcar kernel yields $z_2/z_1 = 0.136$, which is 16 % higher than the Gaussian value of 0.117. This kernel sensitivity arises because the submarine sonar beam pattern (approximately conical) differs from both idealized kernels. The grey envelope in Fig. 5b spans this uncertainty. Kernel dependence is a further reason to prefer the resolution-independent spectral parameters (β_1, β_2, λ_{break}) for quantitative cross-platform comparison.

Over the tested footprint range, the Gaussian-smoothed degradation curve is well described by a power law transfer function:

$$z_2/z_1 = 0.218\,\Delta x^{-0.46}, \quad R^2 = 0.92, \tag{5}$$

where Δx is the effective sensor footprint in metres and the prefactor carries the units required to balance the two sides (Sect. 3.1). The fitted exponent agrees with the value $-(\beta_2 + 3)/2 = -0.46$ predicted analytically from the observed spectral

https://doi.org/10.5194/egusphere-2026-4530
Preprint. Discussion started: 5 November 2026
© Author(s) 2026. CC BY 4.0 License.

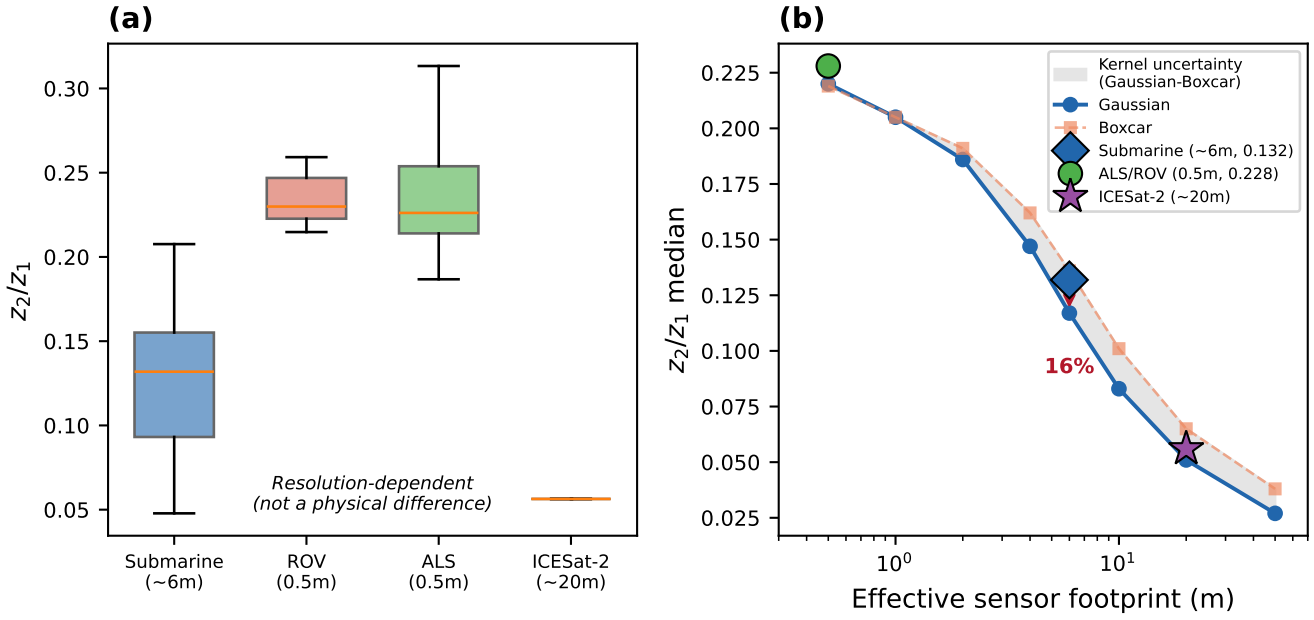


Figure 5. Cross-platform reconciliation of the roughness ratio. (a) Box plots of z_2/z_1 for each platform, showing that the fourfold variation tracks sensor resolution rather than ice morphology. Boxes summarise cruise medians (submarine), flight medians (ALS) and dive medians (ROV); the platform values quoted in the text are medians over all transects and differ from the box centres by less than 0.003. (b) Resolution degradation curve: z_2/z_1 as a function of simulated sensor footprint (Gaussian smoothing of 0.5 m ALS data). Grey shading shows the kernel uncertainty (Gaussian vs. boxcar, 16 % at 6 m). Independent measurements from submarine sonar, ALS/ROV, and ICESat-2 all fall on or near the curve.

shape (Eq. 4), so the curve is anchored in the spectral model rather than fitted freely. Equation (5) allows z_2/z_1 to be predicted at any resolution from a single measurement, and provides a practical tool for inter-calibrating roughness estimates across platforms with different spatial resolutions. The same mechanism operates within the submarine archive alone: z_2/z_1 correlates with the native sampling interval across cruises ($r = -0.64$, $p < 10^{-4}$; Fig. A1a), so sampling resolution shapes the ratio even among instruments of one type.

4.3 Spectral shape over six decades

Having established that z_2/z_1 is resolution-dependent, we use the resolution-independent exponents to test for temporal change. We extracted broken power law parameters (β_1, β_2, λ_{break}) from 5470 ice draft segments across 43 submarine cruises spanning 1960–2005 (Fig. 6). At the cruise-median level ($n = 43$), none of the three spectral parameters exhibits a statistically significant linear trend: β_1 ($r = -0.25$, $p = 0.10$), β_2 ($r = -0.10$, $p = 0.52$), and λ_{break} ($r = -0.38$, $p = 0.012$ for the full sample but $r = -0.23$, $p = 0.15$ after excluding two leveraged 1960 cruises). The two 1960 cruises act as leverage points because of their temporal isolation and their somewhat shallower β_2 values (-1.51 and -1.62 compared with the 1965–2005 median of

https://doi.org/10.5194/egusphere-2026-4530
Preprint. Discussion started: 5 November 2026
© Author(s) 2026. CC BY 4.0 License.

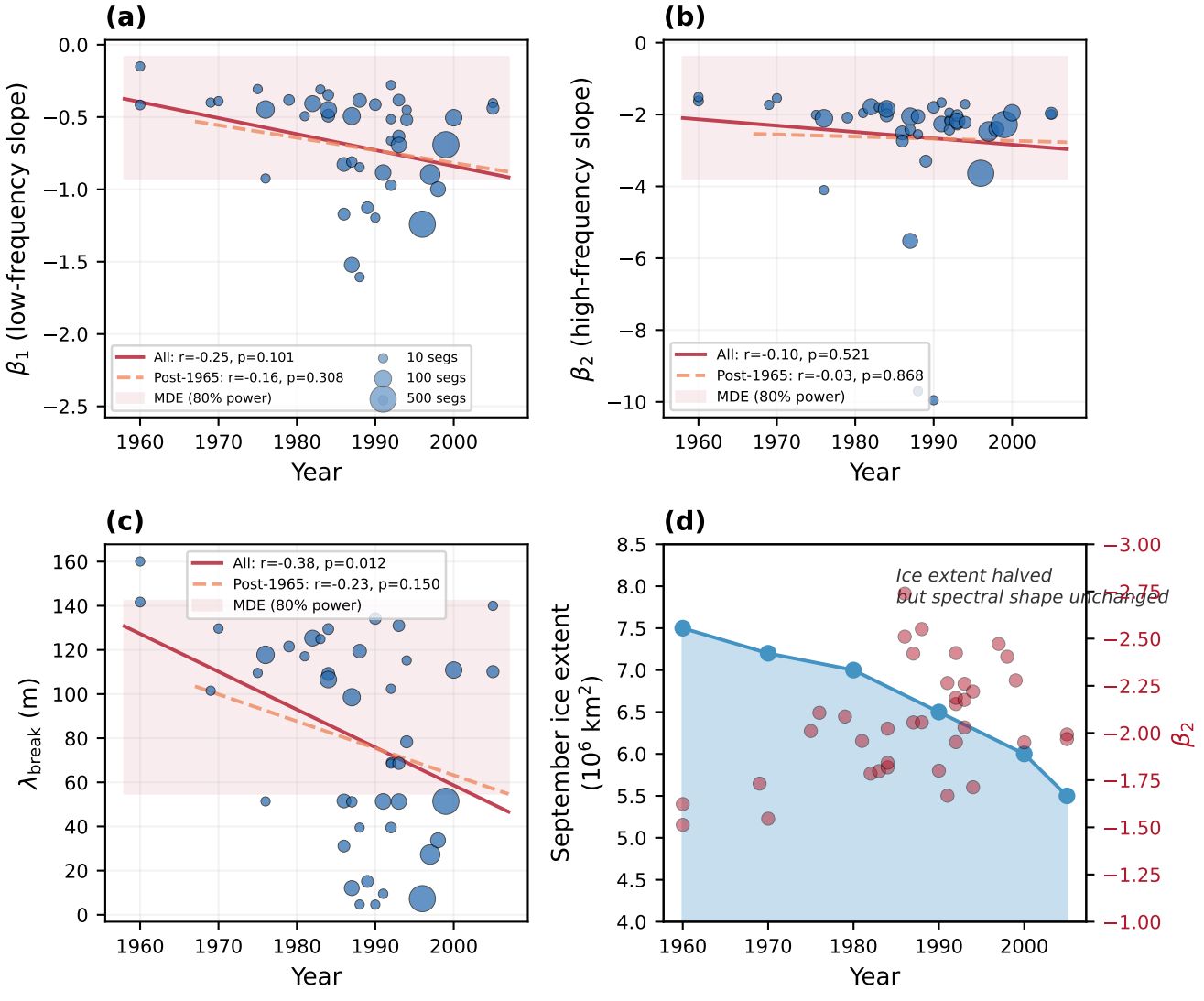


Figure 6. Spectral parameters of submarine ice draft profiles over 1960–2005 (43 cruise-level medians). (a) Low-frequency exponent β_1. (b) High-frequency exponent β_2. (c) Break wavelength λ_{break}. In each panel, solid red lines show the full-sample linear regression and dashed orange lines the regression after excluding two leveraged 1960 cruises. Pink shading indicates the minimum detectable effect at 80 % power. Marker size is proportional to the number of segments per cruise. (d) September Arctic sea ice extent (blue shading) overlaid with β_2 cruise medians (red dots), illustrating the decline of the ice cover over the period in which spectral shape shows no detectable change.

-2.11); removing them eliminates the marginal significance of λ_{break} and further weakens the already non-significant β_1 and β_2 trends. Nonparametric Spearman tests yield marginal monotonic signals for β_1 ($p = 0.024$) and λ_{break} ($p = 0.034$), but not β_2 ($p = 0.066$); none survives Bonferroni correction for three parameters (adjusted threshold $p = 0.017$).

https://doi.org/10.5194/egusphere-2026-4530
Preprint. Discussion started: 5 November 2026
© Author(s) 2026. CC BY 4.0 License.

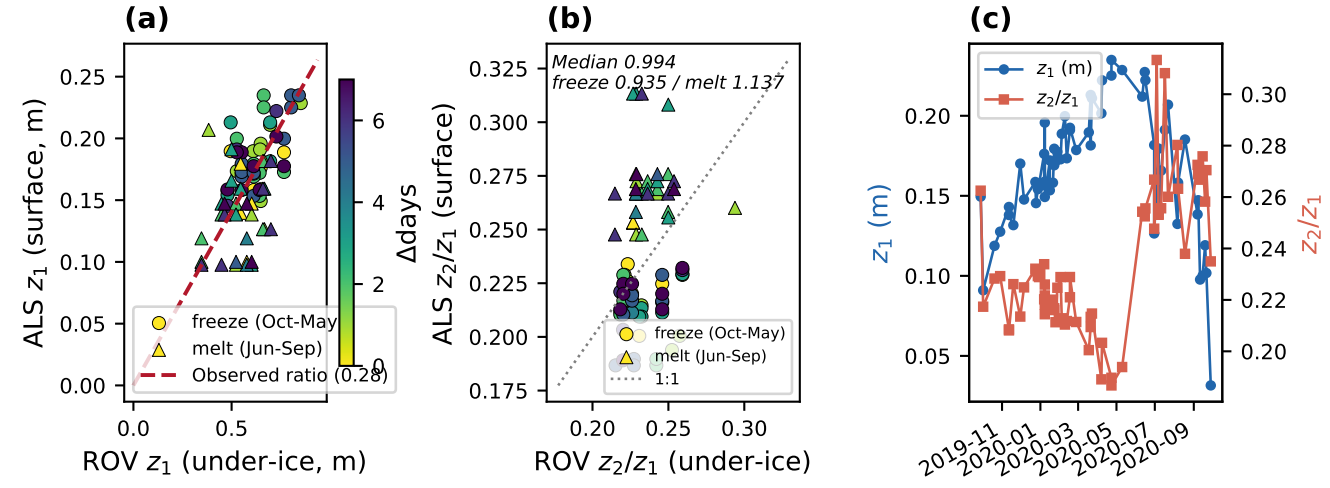


Figure 7. Surface–bottom isostatic fidelity and seasonal evolution. (a) ALS surface z_1 versus ROV under-ice z_1 for 85 paired observations; the dashed line shows the observed ratio of 0.28, about twice the snow-free isostatic expectation. (b) ALS versus ROV z_2/z_1 with 1:1 line; the median ratio of 0.99 indicates that isostasy holds at the derivative level over the year as a whole, but freeze-season pairs (circles, 0.94) lie below the 1:1 line and melt-season pairs (triangles, 1.14) above it. Colour indicates the time separation between paired observations. (c) Seasonal evolution of z_1 (blue, left axis) and z_2/z_1 (red, right axis) from 63 MOSAiC ALS flights spanning September 2019 to September 2020.

During this same 45-year period, September Arctic sea ice extent decreased from approximately 7.5 to 5.5 million km^2, and mean ice thickness declined by roughly half (Kwok, 2018) (Fig. 6d). The null result must be read together with the detection limit of the archive. Power analysis indicates that the minimum detectable trend at 80 % power ($\alpha = 0.05$, two-sided) corresponds to a total β_2 change of 3.37 over 45 years, equivalent to about 160 % of the median absolute value. The submarine record therefore constrains the spectral exponents only against changes of that magnitude: it rules out a catastrophic reorganization of the roughness spectrum, but it cannot exclude slow drifts of tens of percent. Segment-level box-whisker plots grouped by decade show overlapping interquartile ranges for both β_1 and β_2 (Fig. A2). The uneven temporal sampling of the archive (Sect. 2) further limits the power to detect trends at the extremes of the time series.

4.4 Isostatic fidelity at the derivative level and its seasonal breakdown

Paired comparison of 85 quasi-simultaneous ALS–ROV observations (±7 days, <50 km separation) spanning December 2019 to September 2020 shows that the surface-to-bottom ratio of z_1 is 0.28 ± 0.06 (median ± standard deviation over pairs; Fig. 7a). For snow-free ice in isostatic balance the expected ratio of freeboard to draft variations is $(\rho_{\mathrm{water}} - \rho_{\mathrm{ice}})/\rho_{\mathrm{ice}} \approx 0.11$–$0.17$ for typical sea ice densities of 880–920 kg m^{-3}. The observed value is about twice this expectation, consistent with snow accumulation adding surface roughness that has no counterpart at the underside.

https://doi.org/10.5194/egusphere-2026-4530
Preprint. Discussion started: 5 November 2026
© Author(s) 2026. CC BY 4.0 License.

The corresponding ratio of z_2/z_1 is 0.99 ± 0.14 over the 85 pairs, and 0.99 when the pairs are first aggregated to one value per ROV dive ($n = 28$), which is the appropriate treatment given that each dive contributes 1–7 pairs (Sect. 3.5). The ratio is thus within 1 % of unity while the z_1 ratio for the same pairs is 0.28 (Fig. 7b). This is the behaviour expected from isostatic theory: if the surface profile is a linear scaling of the bottom profile, the ratio z_2/z_1 is preserved exactly while the ratio of z_1 is not. The isostatic approximation therefore extends beyond bulk height statistics to the first spatial derivative of the ice surface, which is the condition required for satellite-measured surface roughness to be mapped onto under-ice morphology.

The full-year median conceals a seasonal contrast that the pairs are now numerous enough to resolve. In the freeze season (October–May, $n = 51$) the ratio is 0.94 ± 0.07, the surface being marginally smoother than the underside, consistent with snow infilling between ridges and with lateral density heterogeneity within ridge rubble, both of which break the strict proportionality between the two surfaces. In the melt season (June–September, $n = 34$) the ratio reverses to 1.14 ± 0.10: the surface becomes measurably *sharper* than the underside (Fig. 7b, triangles). Two processes could produce this, acting on opposite faces of the ice: melt ponds and differential surface ablation adding high-frequency structure above that has no isostatic counterpart, and basal melt smoothing the underside below. Our observations constrain their combined effect but do not separate them, and filtering low-freeboard pixels shows that ponds alone do not account for the melt-season signal (Fig. S8). Derivative-level isostatic fidelity is therefore a freeze-season property, holding to 6 % from October to May and failing by 14 % at the height of the melt season. Satellite roughness retrievals that assume a fixed surface-to-bottom relation should be restricted to the freeze season, or carry a seasonally varying correction.

4.5 Seasonal modulation of amplitude but not shape

The 63-flight ALS time series spanning September 2019 to September 2020 captures the full freeze-up to melt-onset cycle (Fig. 7c). The roughness amplitude z_1 increases steadily from $\sim$0.09 m during early autumn freeze-up to a midwinter maximum of $\sim$0.21 m, consistent with progressive ridge formation and snow accumulation. It then falls through the melt season and reaches 0.032 m in the final September flights, so that over the year as a whole z_1 spans 0.032–0.235 m, a factor of seven. Over the same year z_2/z_1 spans only 0.187–0.313, a factor of 1.7, and within the freeze season (October–May) it is confined to 0.187–0.234; through midwinter (December–March) it holds at 0.200–0.234 with a median of 0.219. The remaining variation is concentrated in the melt season, when the surface becomes a heterogeneous mixture of bare ice, melt ponds, and residual snow. Because all flights share the same 0.5 m grid, this comparison is free of the resolution artefact of Sect. 4.2.

The same decoupling appears in the ICESat-2 record. Across seven sampling windows spanning five freeze seasons (2018–2023; 8878 transects), z_2/z_1 remains within 0.057–0.077 while z_1 varies eightfold (0.012–0.100 m; Fig. S9). Amplitude and shape thus respond differently to forcing at the intra-annual timescale, mirroring the absence of a detectable multi-decadal trend in the spectral exponents of the submarine record.

https://doi.org/10.5194/egusphere-2026-4530
Preprint. Discussion started: 5 November 2026
© Author(s) 2026. CC BY 4.0 License.

5 Discussion

5.1 Using the transfer function for cross-platform inter-calibration

The immediate consequence of Sect. 4.2 is that published roughness ratios cannot be compared between platforms at face value. A z_2/z_1 of 0.22 from a 0.5 m ALS grid and one of 0.06 from ICESat-2 are not in conflict; they are the same surface viewed through different bandwidths. Equation (5) converts between them, with the kernel envelope of Fig. 5b ($\sim$16 % at a 6 m footprint) setting the accuracy of that conversion. Two caveats apply. First, the transfer function is calibrated on MOSAiC ALS grids and inherits their ice regime; extending it to markedly different ice covers requires re-checking the underlying β_2. Second, it is a relation between *effective* footprints, and effective footprint is not always the nominal instrument specification. For ICESat-2 ATL07 the effective footprint ($\sim$20 m) exceeds the nominal segment spacing (6.8 m) because the segment-fitting algorithm averages over $\sim$150 photons. Where an effective footprint is unknown, the resolution-independent exponents β_1, β_2, and λ_{break} should be used instead.

For satellite altimetry, the degradation curve provides a link between the roughness measured at the satellite footprint scale and the intrinsic morphology at finer scales. Combined with the isostatic fidelity demonstrated at the derivative level (Fig. 7a, b), this enables under-ice morphological parameters to be inferred from surface measurements alone, and offers a route to reducing the 20–30 % thickness retrieval errors attributed to inadequate roughness assumptions (Landy et al., 2020). The seasonal breakdown of that fidelity (Sect. 4.4) bounds where the inference is safe: freeze-season retrievals can use a fixed surface-to-bottom relation, whereas summer retrievals cannot, which happens to coincide with the period in which altimetric freeboard is least reliable for other reasons. The growing ICESat-2 record (2018–present) makes it possible to monitor z_2/z_1 at basin scale with near-monthly cadence; the degradation curve supplies the calibration anchor such monitoring requires.

The result also has a practical implication for sea ice models. Current climate models prescribe a single roughness length scale. The two-regime spectral description separates a stable morphological "shape" from a time-varying "amplitude", so that only the amplitude parameter z_1 needs dynamic adjustment, which can in turn be linked to more readily observable quantities such as ice thickness or concentration. We note that this simplification is licensed only to the accuracy of the detection bound in Sect. 4.3: it is a statement that no large change in the exponents has been observed, not a demonstration that they are exactly constant.

5.2 Why spectral shape is insensitive to thinning

The decoupling of spectral shape from ice volume is consistent with the physics of pressure ridge formation. Ridging occurs when converging ice plates fracture into discrete blocks that pile up under the combined action of the driving force, gravity, and inter-block friction (Hopkins, 1998; Parmerter and Coon, 1972; Timco and Weeks, 2010). Each of these governing factors, the flexural strength of the ice, gravitational acceleration, and the internal friction angle of rubble, is either a material constant or varies only weakly with ice thickness. More broadly, atomistic simulations of plastically deformed solids show that spatially correlated deformation produces self-affine roughness whose Hurst exponent is set by how correlated the deformation events are rather than by the total strain (Hinkle et al., 2020). In this framework, z_1 records how much deformation has occurred, while

https://doi.org/10.5194/egusphere-2026-4530
Preprint. Discussion started: 5 November 2026
© Author(s) 2026. CC BY 4.0 License.

β_1 and β_2 encode how that deformation is organized across scales. Thinning of the Arctic ice cover reduces the amplitude of ridging but need not alter the fracture mechanics that shape its spectral character.

5.3 Reconciliation with observed surface smoothing

Recent airborne laser observations report a progressive smoothing of the Arctic ice surface over the past three decades, attributed to the loss of deformed multi-year ice (Krumpen et al., 2025). That finding is not in conflict with the results reported here. The reported smoothing manifests primarily as a decline in z_1 (roughness amplitude), which our analysis confirms is climate-sensitive at both seasonal and multi-decadal timescales. The spectral exponents, by contrast, describe the relative distribution of roughness across scales, and show no detectable change. Together the two results imply that the Arctic ice cover is becoming uniformly quieter across all wavelengths while retaining its spectral shape, akin to turning down the volume without changing the instrument. The five-season ICESat-2 sample (Sect. 4.5) extends this decoupling of shape from amplitude into the satellite era, although five seasons is far too short to constitute a trend test in its own right.

5.4 A possible shift in the break wavelength

Although β_1 and β_2 show no significant trend, λ_{break} exhibits a marginal Spearman correlation with time ($p = 0.034$), suggesting a possible shortening from $\sim$140 m in the 1960s to $\sim$110 m by the 2000s. This signal is sensitive to the two earliest cruises and does not survive a leave-out robustness test based on Pearson regression ($p = 0.15$). A partial correlation controlling for sampling interval d_x strengthens rather than weakens the signal ($r = -0.42$, $p = 0.005$), confirming that the marginal trend is not an instrument artefact, but it remains non-significant after excluding the 1960 leverage points ($r = -0.27$, $p = 0.08$). Physically, a shortening of λ_{break} would be consistent with the disappearance of the largest multi-year ridge systems and a shift toward smaller, more frequent deformation features, the "big ridges decrease, small obstacles increase" pattern documented by Castellani et al. (2014). If confirmed with higher-cadence data such as the growing ICESat-2 record (Markus et al., 2017; Duncan and Farrell, 2022), this would indicate that the spectral shape undergoes a slow reorganization of energy across scales while preserving its slope parameters. We regard it as the most promising target for a future test, not as an established trend.

5.5 Relation to fracture roughness in other materials

The values of the exponents invite a comparison beyond sea ice. Multi-instrument studies of earthquake fault surfaces have shown that roughness measured across nine orders of magnitude in scale collapses onto a single self-affine model with exponents that are independent of fault maturity, slip history, and host rock lithology (Candela et al., 2012). Molecular-dynamics simulations of compressed metals, alloys, and metallic glasses indicate that spatially correlated plastic deformation produces self-affine surfaces whose Hurst exponent reflects how correlated the deformation events are rather than the total accumulated strain (Hinkle et al., 2020). The high-frequency spectral exponent of Arctic sea ice ($\beta_2 \approx -2.2$, equivalent to a Hurst exponent $H = 0.59$; cluster-bootstrap 95 % CI 0.53–0.74) is consistent with the slip-parallel roughness of fault surfaces ($H_{\parallel} = 0.58 \pm 0.07$; Candela et al. 2012) and falls within the $H = 0.5$–0.8 range associated with correlated plastic deformation

https://doi.org/10.5194/egusphere-2026-4530
Preprint. Discussion started: 5 November 2026
© Author(s) 2026. CC BY 4.0 License.

of solids (Hinkle et al., 2020). Under cluster-bootstrap weighting the confidence interval excludes both a Brownian profile ($H = 0.5$) and the low-exponent brittle-fracture class reported for compacted-grain sandstone ($\zeta = 0.46 \pm 0.05$; Ponson et al. 2007). Neither exclusion survives a change of weighting. With equal cruise weighting (median of cruise medians, $H = 0.54$, 95 % CI 0.50–0.63) the lower bound touches the Brownian value, and it also overlaps the upper end of the sandstone interval. The comparison therefore places sea ice above the sandstone class and at or above the Brownian value under both weightings, but only the cluster-bootstrap estimate separates it from them with confidence (Fig. S4).

Two limits on this comparison should be stated plainly. It rests on the agreement of a single exponent, which is a necessary but not a sufficient condition for a shared mechanism, and the low-frequency exponent ($\beta_1 \approx -0.5$) has no counterpart in the geological measurements: it reflects the spatial clustering of ridges and keels at wavelengths above the break scale, a mesoscale organization imposed by the kinematics of ice plate convergence rather than by the fracture process itself. We therefore present the agreement as a consistency worth testing further, for example against directional roughness statistics or ridge-scale block-size distributions, rather than as evidence that sea ice belongs to an established universality class.

5.6 Snow, melt ponds, and what the ALS surface represents

The ALS instrument measures freeboard (snow plus ice above water level) rather than bare ice surface elevation, and snow redistribution (sastrugi, wind slabs) could in principle contribute its own spectral signature to the high-frequency regime. The close agreement between the ALS surface ($z_2/z_1 = 0.226$) and the ROV under-ice value ($z_2/z_1 = 0.232$) at the same 0.5 m resolution, combined with a freeze-season surface-to-bottom ratio of 0.94, indicates that snow does not dominate the spectral shape. If wind-driven snow features contributed substantially, the surface spectrum would be steeper or noisier than the draft spectrum at high frequencies. Instead the freeze-season surface is marginally the smoother of the two, as expected if snow preferentially fills the hollows between ridges. Definitive separation of ice and snow contributions would require coincident snow radar measurements.

The melt season is a genuine exception rather than a caveat about noise. Aggressive filtering of low-freeboard ALS pixels ($h_{\mathrm{fb}} > 0.15$ m) still leaves a ∼6 % increase in z_2/z_1 during June–August (Fig. S8), and the paired ROV comparison independently shows the surface becoming 14 % sharper than the underside over the same months. Two instruments on opposite sides of the ice therefore agree that summer modifies the surface specifically, not the ice as a whole. The stability of the shape parameters documented here, and the derivative-level isostatic relation that follows from it, are best understood as freeze-season (October–May) properties.

6 Conclusions

The factor-of-four variation in the roughness ratio z_2/z_1 among submarine sonar, ROV multibeam, airborne laser scanning, and satellite photon-counting lidar is a bandwidth effect, not a geophysical one. All four platforms fall on a single resolution degradation curve, $z_2/z_1 = 0.218\,\Delta x^{-0.46}$ ($R^2 = 0.92$), whose exponent follows analytically from the observed broken power law spectrum rather than being fitted freely. This transfer function allows roughness estimates from platforms with effective

https://doi.org/10.5194/egusphere-2026-4530
Preprint. Discussion started: 5 November 2026
© Author(s) 2026. CC BY 4.0 License.



footprints between 0.5 and 20 m to be inter-calibrated, to an accuracy set by the $\sim$16 % smoothing-kernel uncertainty and within the ice regime of the MOSAiC grids on which it is calibrated. The underlying spectral shape, described by $\beta_1 \approx -0.5$, $\beta_2 \approx -2.2$, and $\lambda_{\mathrm{break}} \approx 99$ m, is common to all four platforms and to both ice surfaces.

Applied to the submarine archive, the resolution-independent exponents show no statistically significant trend over 43 cruises spanning 1960–2005, a period in which mean ice thickness roughly halved. What that null result licenses is bounded in three ways. The archive constrains it to changes smaller than about 160 % of the median exponent at 80 % statistical power, so it rules out a catastrophic reorganization of the roughness spectrum but not a slow drift of tens of percent, and the uneven temporal sampling of the cruises weakens the bound further at both ends of the record. It is a statement about the parameters a one-dimensional spectrum can see, which excludes the preferential orientation of ridges, regional contrasts that cancel in cruise-level medians, and the shape of individual keel cross-sections. And it stops in 2005: the two most recent decades of Arctic change rest on the much shorter ICESat-2 sample. Within those bounds the break wavelength shows a marginal shortening that does not survive removal of two leverage cruises, and it remains the most promising target for a future test. Over the seasonal cycle the same decoupling is visible directly: through the MOSAiC year z_1 varies sevenfold (0.032–0.235 m) while z_2/z_1 spans only 0.187–0.313, and stays within 0.19–0.23 for the whole freeze season.

Eighty-five paired surface–bottom observations spanning a full MOSAiC year show that the isostatic approximation holds at the derivative level, with a z_2/z_1 surface-to-bottom ratio of 0.99 ± 0.14 (0.99 aggregated to the 28 contributing ROV dives) against 0.28 for the amplitude z_1. The fidelity is seasonal: 0.94 ± 0.07 from October to May, reversing to 1.14 ± 0.10 from June to September, when melt ponds and differential ablation make the surface sharper than the underside. Freeboard-based inference of under-ice morphology is therefore reliable in the freeze season and requires a seasonal correction in summer. This result rests on a narrower base than the pair count suggests, since the 85 pairs derive from 28 ROV dives and 45 ALS flights on a single drifting floe system over one annual cycle, with the melt-season contrast carried by the smaller subset of 34 pairs from 12 dives. It is established for MOSAiC ice and awaits confirmation where pond fraction and basal melt rates differ, particularly in the first-year ice of the marginal seas.

Combined with the resolution transfer function, the derivative-level isostatic relation makes it possible to infer under-ice morphological parameters from satellite surface measurements, and opens a route to replacing single-parameter roughness assumptions in freeboard-to-thickness conversion with a two-parameter spectral description in which only the amplitude requires dynamic updating. Two lines of work would sharpen it. Continued ICESat-2 analysis can extend the temporal baseline, testing whether the exponents remain stable under further warming and whether the marginal break-wavelength signal is real. Two-dimensional Fourier analysis of the high-resolution ALS and ROV grids can characterize the directional organization of ridges, which one-dimensional spectra cannot resolve and which the present null result therefore does not constrain.

https://doi.org/10.5194/egusphere-2026-4530
Preprint. Discussion started: 5 November 2026
© Author(s) 2026. CC BY 4.0 License.

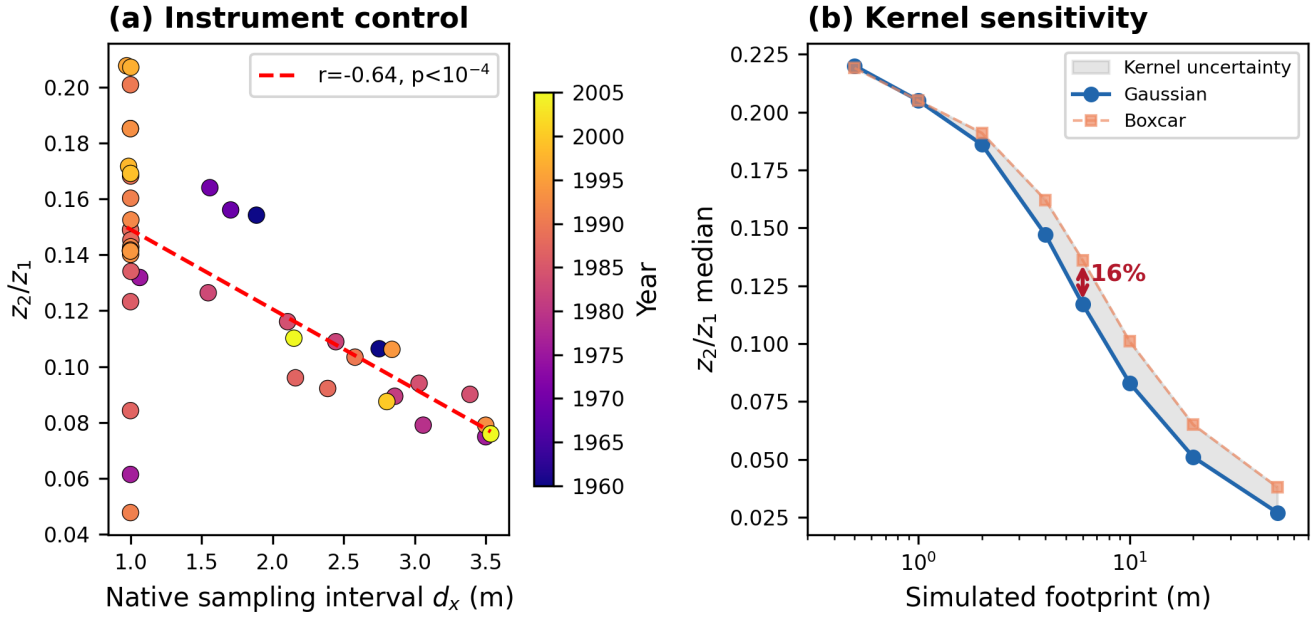


Figure A1. Instrument control and kernel sensitivity. (a) Cruise-median z_2/z_1 versus native sampling interval d_x, showing a strong correlation ($r = -0.64$, $p < 10^{-4}$) that confirms z_2/z_1 differences among cruises are partly instrumental. Colour indicates cruise year. (b) Resolution degradation curves for Gaussian and boxcar smoothing kernels applied to 0.5 m ALS data. The 16 % difference at a 6 m footprint (annotated) establishes the kernel-dependent uncertainty envelope for cross-platform z_2/z_1 comparisons.

Appendix A: Supporting analyses

Code and data availability. Submarine ice draft profiles are available from NSIDC (G01360; https://nsidc.org/data/g01360). MOSAiC ALS data are available from PANGAEA (https://doi.org/10.1594/PANGAEA.950339). MOSAiC ROV multibeam data are available from PANGAEA (https://doi.org/10.1594/PANGAEA.971872). ICESat-2 ATL07 version 007 data are available from NSIDC (https://doi.org/10.5067/ATLAS/ATL07.007). All analysis scripts are available at https://github.com/yangleir/TC_ice. The supplement contains nine supporting figures (S1–S9) documenting the broken power law null test, bin-count sensitivity, the analytic basis of the degradation curve, the Hurst cluster bootstrap, and the instrument, regional, segment-length, melt-pond, and multi-season robustness checks.

Author contributions. L.Y. conceived the study, performed the analysis, and wrote the manuscript. L.Z. contributed to data processing and interpretation.

https://doi.org/10.5194/egusphere-2026-4530
Preprint. Discussion started: 5 November 2026
© Author(s) 2026. CC BY 4.0 License.

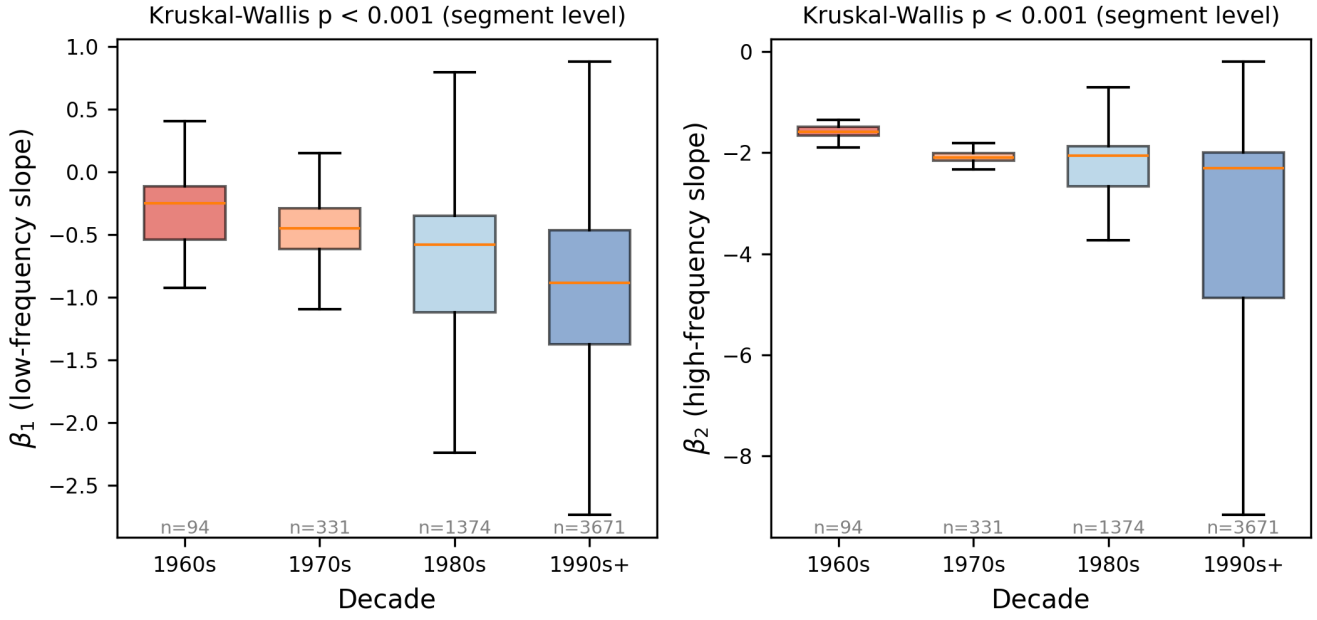


Figure A2. Box-whisker plots of spectral exponents grouped by decade (segment-level data). (a) Low-frequency exponent β_1. (b) High-frequency exponent β_2. Box interquartile ranges overlap across all decade bins (1990s and 2000s merged). The segment-level Kruskal–Wallis significance ($p < 0.001$) is inflated by within-cruise autocorrelation; the decisive cruise-median comparison (Fig. 6) shows no significant trend. Numbers below each box indicate the segment count per bin.

Competing interests. The authors declare that they have no competing interests.

Acknowledgements. We thank the crews of the US, UK, and SCICEX submarines for collecting ice draft data over six decades, the MOSAiC expedition participants for ALS and ROV operations, and the NASA ICESat-2 Science Team for the satellite data products. MOSAiC was supported by the Alfred Wegener Institute Helmholtz Centre for Polar and Marine Research.

https://doi.org/10.5194/egusphere-2026-4530
Preprint. Discussion started: 5 November 2026
© Author(s) 2026. CC BY 4.0 License.

References

Anhaus, P., Arndt, S., Katlein, C., Krampe, D., Lange, B. A., Matero, I., Regnery, J., Rohde, J., Schiller, M., and Nicolaus, M.: Multibeam sea-ice draft from remotely operated vehicle (ROV) surveys during the MOSAiC expedition 2019/20, version 2.0, PANGAEA, https://doi.org/10.1594/PANGAEA.971872, 2024.

Anhaus, P., Katlein, C., Arndt, S., Krampe, D., Lange, B. A., Matero, I., Salganik, E., and Nicolaus, M.: Under-ice environment observations from a remotely operated vehicle during the MOSAiC expedition, Scientific Data, 12, 944, https://doi.org/10.1038/s41597-025-05223-1, 2025.

Candela, T., Renard, F., Klinger, Y., Mair, K., Schmittbuhl, J., and Brodsky, E. E.: Roughness of fault surfaces over nine decades of length scales, Journal of Geophysical Research: Solid Earth, 117, B08 409, https://doi.org/10.1029/2011JB009041, 2012.

Castellani, G., Lüpkes, C., Hendricks, S., and Gerdes, R.: Variability of Arctic sea-ice topography and its impact on the atmospheric surface drag, Journal of Geophysical Research: Oceans, 119, 6743–6762, https://doi.org/10.1002/2013JC009712, 2014.

Duncan, K. and Farrell, S. L.: Determining variability in Arctic sea ice pressure ridge topography with ICESat-2, Geophysical Research Letters, 49, e2022GL100 272, https://doi.org/10.1029/2022GL100272, 2022.

Eilers, C. and Bradley, A. C.: Characteristic geometry of keels in Arctic sea ice ridges, Geophysical Research Letters, 53, https://doi.org/10.1029/2025GL119003, 2026.

Goff, J. A.: Quantitative analysis of sea ice draft: 1. Methods for stochastic modeling, Journal of Geophysical Research: Oceans, 100, 6993–7004, https://doi.org/10.1029/94JC03200, 1995.

Hinkle, A. R., N"ohring, W. G., Leute, R., Junge, T., and Pastewka, L.: The emergence of small-scale self-affine surface roughness from deformation, Science Advances, 6, eaax0847, https://doi.org/10.1126/sciadv.aax0847, 2020.

Hopkins, M. A.: Four stages of pressure ridging, Journal of Geophysical Research: Oceans, 103, 21 883–21 891, https://doi.org/10.1029/98JC01257, 1998.

Hutter, N., Hendricks, S., Jutila, A., Birnbaum, G., von Albedyll, L., Ricker, R., et al.: Gridded segments of sea-ice or snow surface elevation and freeboard from helicopter-borne laser scanner during the MOSAiC expedition, PANGAEA, https://doi.org/10.1594/PANGAEA.950339, 2023.

Krumpen, T., von Albedyll, L., Bünger, H. J., Castellani, G., Hartmann, J., Helm, V., Hendricks, S., Hutter, N., Landy, J. C., Lisovski, S., Lüpkes, C., Rohde, J., Suhrhoff, M., and Haas, C.: Smoother sea ice with fewer pressure ridges in a more dynamic Arctic, Nature Climate Change, 15, 66–72, https://doi.org/10.1038/s41558-024-02199-5, 2025.

Kwok, R.: Arctic sea ice thickness, volume, and multiyear ice coverage: losses and coupled variability (1958–2018), Environmental Research Letters, 13, 105 005, https://doi.org/10.1088/1748-9326/aae3ec, 2018.

Kwok, R. and Cunningham, G. F.: ICESat over Arctic sea ice: Estimation of snow depth and ice thickness, Journal of Geophysical Research: Oceans, 113, C08 010, https://doi.org/10.1029/2008JC004753, 2008.

Kwok, R. and Rothrock, D. A.: Decline in Arctic sea ice thickness from submarine and ICESat records: 1958–2008, Geophysical Research Letters, 36, L15 501, https://doi.org/10.1029/2009GL039035, 2009.

Kwok, R., Petty, A., Cunningham, G., Markus, T., Hancock, D., Ivanoff, A., Wimert, J., Bagnardi, M., Kurtz, N., and the ICESat-2 Science Team: ATLAS/ICESat-2 L3A Sea Ice Height, Version 7, NASA National Snow and Ice Data Center DAAC, https://doi.org/10.5067/ATLAS/ATL07.007, 2025.

https://doi.org/10.5194/egusphere-2026-4530
Preprint. Discussion started: 5 November 2026
© Author(s) 2026. CC BY 4.0 License.

Landy, J. C., Petty, A. A., Tsamados, M., and Stroeve, J. C.: Sea ice roughness overlooked as a key source of uncertainty in CryoSat-2 ice freeboard retrievals, Journal of Geophysical Research: Oceans, 125, e2019JC015 820, https://doi.org/10.1029/2019JC015820, 2020.

Lindsay, R. and Schweiger, A.: Arctic sea ice thickness loss determined using subsurface, aircraft, and satellite observations, The Cryosphere, 9, 269–283, https://doi.org/10.5194/tc-9-269-2015, 2015.

Luthcke, S. B., Thomas, T. C., Pennington, T. A., Rebold, T. W., Nicholas, J. B., Rowlands, D. D., Gardner, A. S., and Bae, S.: ICESat-2 pointing calibration and geolocation performance, Earth and Space Science, 8, e2020EA001 494, https://doi.org/10.1029/2020EA001494, 2021.

Markus, T., Neumann, T., Martino, A., Abdalati, W., Brunt, K., Csatho, B., Farrell, S., Fricker, H., Gardner, A., Harding, D., Jasinski, M., Kwok, R., Magruder, L., Lubin, D., Luthcke, S., Morison, J., Nelson, R., Neuenschwander, A., Palm, S., Popescu, S., Shum, C. K., Schutz, B. E., Smith, B., Yang, Y., and Zwally, J.: The Ice, Cloud, and land Elevation Satellite-2 (ICESat-2): Science requirements, concept, and implementation, Remote Sensing of Environment, 190, 260–273, https://doi.org/10.1016/j.rse.2016.12.029, 2017.

Martin, T., Tsamados, M., Schroeder, D., and Feltham, D. L.: The impact of variable sea ice roughness on changes in Arctic Ocean surface stress: A model study, Journal of Geophysical Research: Oceans, 121, 1931–1952, https://doi.org/10.1002/2015JC011186, 2016.

Myers, N. O.: Characterization of surface roughness, Wear, 5, 182–189, https://doi.org/10.1016/0043-1648(62)90002-9, 1962.

National Snow and Ice Data Center: Submarine Upward Looking Sonar Ice Draft Profile Data and Statistics, Version 1 (G01360), Boulder, Colorado USA. NSIDC, https://doi.org/10.7265/N54Q7RWK, 1998.

Nicolaus, M., Perovich, D. K., Spreen, G., Granskog, M. A., von Albedyll, L., Angelopoulos, M., et al.: Overview of the MOSAiC expedition: Snow and sea ice, Elementa: Science of the Anthropocene, 10, 000 046, https://doi.org/10.1525/elementa.2021.000046, 2022.

Parmerter, R. R. and Coon, M. D.: Model of pressure ridge formation in sea ice, Journal of Geophysical Research, 77, 6565–6575, https://doi.org/10.1029/JC077i033p06565, 1972.

Petty, A. A., Tsamados, M. C., Kurtz, N. T., Farrell, S. L., Newman, T., Harbeck, J. P., Feltham, D. L., and Richter-Menge, J. A.: Characterizing Arctic sea ice topography using high-resolution IceBridge data, The Cryosphere, 10, 1161–1179, https://doi.org/10.5194/tc-10-1161-2016, 2016.

Ponson, L., Auradou, H., Pessel, M., Lazarus, V., and Hulin, J.-P.: Failure mechanisms and surface roughness statistics of fractured Fontainebleau sandstone, Physical Review E, 76, 036 108, https://doi.org/10.1103/PhysRevE.76.036108, 2007.

Rothrock, D. A. and Thorndike, A. S.: Geometric properties of the underside of sea ice, Journal of Geophysical Research: Oceans, 85, 3955–3963, https://doi.org/10.1029/JC085iC07p03955, 1980.

Rothrock, D. A., Percival, D. B., and Wensnahan, M.: The decline in arctic sea-ice thickness: Separating the spatial, annual, and interannual variability in a quarter century of submarine data, Journal of Geophysical Research: Oceans, 113, C05 003, https://doi.org/10.1029/2007JC004252, 2008.

Stroeve, J. and Notz, D.: Changing state of Arctic sea ice across all seasons, Environmental Research Letters, 13, 103 001, https://doi.org/10.1088/1748-9326/aade56, 2018.

Timco, G. W. and Weeks, W. F.: A review of the engineering properties of sea ice, Cold Regions Science and Technology, 60, 107–129, https://doi.org/10.1016/j.coldregions.2009.10.003, 2010.

Tsamados, M., Feltham, D. L., Schroeder, D., Flocco, D., Farrell, S. L., Kurtz, N., Laxon, S. W., and Bacon, S.: Impact of variable atmospheric and oceanic form drag on simulations of Arctic sea ice, Journal of Physical Oceanography, 44, 1329–1353, https://doi.org/10.1175/JPO-D-13-0215.1, 2014.

https://doi.org/10.5194/egusphere-2026-4530
Preprint. Discussion started: 5 November 2026
© Author(s) 2026. CC BY 4.0 License.



510 Wadhams, P. and Horne, R. J.: An analysis of ice profiles obtained by submarine sonar in the Beaufort Sea, Journal of Glaciology, 25, 401–424, https://doi.org/10.3189/S0022143000015264, 1980.